PAPER

Check for updates

Hybrid poly(ionic liquid)/polyhedral oligomeric silsesquioxane artificial solid electrolyte interphase for lithium metal batteries

Wei-Ting Chou,[a] Thi-Ngoc Pham, [iD][a] Ta-Ching Yang,[a] Yun-Jie Tsai,[a] Hsisheng Teng [iD][ac] and Jeng-Shiung Jan [iD] *[abc]

Lithium metal is regarded as a promising anode material for next-generation batteries due to its high theoretical capacity and low electrochemical potential. However, challenges such as unstable solid electrolyte interfaces (SEIs) and uncontrolled dendrite growth can result in irreversible capacity loss and safety hazards. In this work, a pre-formed artificial solid electrolyte interface (ASEI) is constructed on lithium metal by *in situ* polymerization of an imidazole-based poly(ionic liquid) (Im-IL) and polyhedral oligomeric silsesquioxane (POSS) directly on the lithium surface during a pre-assembly treatment step; in this context, the ASEI refers to this conformal polymeric interfacial coating rather than a layer generated solely by spontaneous Li-electrolyte reactions. The resulting organic–inorganic hybrid polymer layer enhances interface adhesion, simplifies processing, and effectively accommodates volume fluctuations during lithium-ion intercalation and deintercalation, resulting in the modified Im-IL/POSS@Li exhibiting a wide electrochemical stability window and remarkable cycling performance. The Im-IL/POSS@Li|LFP cells in carbonate-based electrolyte show superior capacity retention and lower impedance *versus* bare Li|LFP, achieving 94.7% capacity retention after 500 cycles and 84.6% after 1000 cycles. Moreover, in an ether-based electrolyte, the Im-IL/POSS@Li|LFP cells achieve 99.6% capacity retention after 200 cycles, compared to only 26.9% for the unmodified counterpart. XPS and SEM analyses reveal suppressed lithium salt decomposition and the formation of a dense, conductive interphase on Im-IL/POSS@Li. These results demonstrate that the proposed ASEI strategy not only stabilizes lithium metal anodes but also offers a practical pathway toward safe and longer-lasting high-energy-density batteries.

1. Introduction

To improve operating voltage and energy density and reduce size, researchers are seeking optimal materials for both cathodes and anodes. Lithium metal, with its high specific and volumetric capacities and low electrochemical potential (−3.04 V), has driven advancements in battery technology. Nevertheless, its practical application is limited by challenges such as low coulombic efficiency and the formation of lithium dendrites. Lithium metal passivation was first observed in the early 1970s, and in 1979, Peled introduced the concept of the solid electrolyte interphase (SEI),[1] spurring extensive studies on its composition and function. By the 1980s, Li_2CO_3 was

identified as a major SEI component,[2] and Peled later proposed a mosaic model and equivalent circuit representation in 1997.[3] Over time, *in situ* AFM and SEM investigations provided three-dimensional insights into SEI morphology,[4,5] while quantum chemical simulations in the 21st century further clarified SEI formation mechanisms during electrolyte reduction.[6]

As the critical role of the SEI in battery performance became evident, efforts to artificially control its formation emerged. In this context, artificial solid electrolyte interphases (ASEIs) have been developed as pre-engineered, compositionally tunable interfacial layers on Li metal. One approach involves introducing electrolyte additives that decompose during initial charge–discharge cycles to form a stable SEI layer,[7–9] while another strategy employs electrolytes with specialized anions or cations, such as LiFSI, to stabilize SEI formation.[10] Surface coatings offer additional protection by directly modifying the electrode or cathode material,[11–14] with spin coating frequently used to deposit uniform films.[15,16] Techniques such as chemical vapor deposition (CVD) and atomic layer deposition (ALD)[17–20] are also widely employed to fabricate robust ASEI layers. Advances in composite polymer–inorganic electrolytes, such as those incorporating PVDF-HFP with LATP and CeO_2, have been

[a]Department of Chemical Engineering, National Cheng Kung University, Tainan 70101, Taiwan. E-mail: jsjan@mail.ncku.edu.tw; Fax: +886-6-2757575; Tel: +886-6-2757575, ext. 62660

[b]Program on Smart and Sustainable Manufacturing, Academy of Innovative Semiconductor and Sustainable Manufacturing, National Cheng Kung University, Tainan, 70101, Taiwan

[c]Center for Resilience and Intelligence on Sustainable Energy Research (RiSER), National Cheng Kung University, Tainan, 70101, Taiwan

shown to effectively suppress lithium dendrite growth and improve interfacial stability in lithium metal batteries, further enhancing overall battery performance.[21] In the present work, the term ASEI specifically refers to a pre-formed artificial interphase that is constructed on Li metal before cycling, rather than a layer formed solely by spontaneous Li-electrolyte reactions.

Ionic liquids (ILs) are composed of various anions and cations, with the cations typically being large organic molecules and the anions being smaller inorganic species. This size asymmetry results in relatively weak coulombic interactions, allowing ILs to remain liquids at temperatures below 100 °C. In contrast, conventional salts possess stronger ionic bonds, leading to much higher melting points, often near 1000 °C, which limits their practical applications.[22] ILs offer several advantages, including low volatility, high thermal stability, and excellent ionic conductivity due to high ionic mobility, making them highly attractive for electrochemical applications. Key uses include serving as media for electrochemical reactions, such as electrochemical synthesis, electrodeposition, electrolysis, and the fabrication of electrochemical sensors.[23–26]

Beyond their role as reaction media, ILs are also employed as electrolytes[27–30] or as additives to conventional electrolytes to enhance ionic conductivity and chemical stability.[31–37] They are also incorporated into electrode materials,[38] either directly or as surface modifiers, improving ion transport and diffusion rates and thereby enhancing electrochemical performance metrics such as capacitance. With the development of artificial solid electrolyte interphase (ASEI) technologies, ILs have increasingly been integrated into ASEI systems,[39–41] where they contribute to improved interfacial stability and electrochemical efficiency.

Polyhedral oligomeric silsesquioxanes (POSSs) are a class of organic–inorganic hybrid materials featuring a cage-like polyhedral structure composed of silicon and oxygen atoms, with the general formula $(R–SiO_{1.5})_n$, where n typically equals 6, 8, or 10, and R denotes various organic substituents. POSSs are distinguished by their well-defined cage architecture, nanoscale porosity, and versatile surface functionality, making it suitable for a wide range of commercial applications.[42–44] The incorporation of silicon atoms endows POSSs with excellent thermal stability,[45] which has been widely exploited to improve the heat resistance of polymer matrices. Moreover, POSSs have been reported to facilitate ion conduction and enhance electrochemical performance when incorporated into solid-state electrolytes.[46–51] Owing to their unique hollow rigid structure and inorganic cubic siloxane backbone, POSSs are used to modify various properties of polymer matrices, making them a valuable component in ASEI layers.[52,53]

In ASEI design, the interphase must exhibit sufficient mechanical toughness to accommodate volumetric changes induced by lithium dendrite growth, while maintaining high ionic conductivity for effective ion transport. To achieve this balance, flexible ionic liquids (ILs), particularly imidazolium-based cations paired with the highly conductive bis(trifluoromethylsulfonyl)imide (TFSI) anion, are employed. Two different IL backbones poly(ethylene glycol) (PEG$_{200}$) and dodecane are explored to tailor flexibility and conductivity.

POSSs are incorporated to reinforce mechanical strength, which can otherwise be compromised by the softer IL matrix. Acting in concert, the liquid-like IL and cubic structure of the POSS network form continuous ionic pathways within a mechanically robust scaffold. In our system, this hybrid PIL/POSS network is constructed as a conformal coating on the Li metal surface *via* radical *in situ* polymerization during a pre-assembly treatment step; thus, the resulting PIL/POSS layer constitutes a pre-formed ASEI that tightly adheres to the Li surface and minimizes interfacial gaps and is designed to suppress dendrite growth and improve interfacial stability.

2. Experimental

2.1. Materials

Poly(ethylene glycol) (PEG$_{200}$, molecular weight (M_n): 200 g mol^{-1}, SHOWA), phosphorus tribromide (99%, Acros), chloroform (SeedChem), magnesium sulfate anhydrous (Avantor), charcoal activated (TCI), 1-vinylimidazole (99%, Alfa), 1,12-dibromododecane (Acros), ethyl acetate (DUKSAN), lithium bis(trifluoromethanesulfonyl)imide (LiTFSI, 99.9%, Solvay), PSS-octavinyl substituted (POSS, MACKLIN), tetrahydrofuran (THF, DUKSAN), polyvinylidene difluoride (PVDF, Arkema), N-methyl-2-pyrrolidone (NMP, Macron), Super-P (SP, Timcal), lithium iron phosphate (LiFePO$_4$, LFP, Aleees), and 2,2′-azobis(2-methylpropionitrile) (AIBN, Aencore) were used. Lithium nitrate (LiNO$_3$), 1,3-dioxolane (DOL), and dimethyl ether (DME) were bought from Sigma-Aldrich. Lithium metal with a 15.6 mm diameter was supplied by New Battery Energy. Lithium bis(trifluoromethylsulphonyl)imide (LiTFSI), a CR2032 coin cell, and aluminum foil were purchased from UBIQ. The electrolyte (1 M LiPF6 in EC : DEC with a 1 : 1 volume ratio) was obtained from UBIQ, and the separator (D3182) was sourced from BenQ.

2.2. Synthesis of Br-PEG$_{200}$-Br

As illustrated in the Scheme S1a, Br-PEG$_{200}$-Br was synthesized by reacting 35 g of PEG$_{200}$ (0.175 mol) and 63.3 g of PBr$_3$ (0.234 mol). Both reagents were dissolved separately in chloroform, and the PBr$_3$ solution was added dropwise to the PEG$_{200}$ solution under an ice bath. The reaction mixture was stirred for 2 days. After completion, the excess PBr$_3$ was extracted with deionized (DI) water three times. The organic layer was subsequently purified using activated charcoal and anhydrous magnesium sulfate and then concentrated under reduced pressure to obtain a transparent Br-PEG$_{200}$-Br liquid.

2.3. Synthesis of [VIm-PEG$_{200}$-VIm][TFSI]

The synthesis of the ionic liquid is shown in Scheme S1b. Br-PEG$_{200}$-Br (29.1 g, 0.091 mol) was dissolved in ethyl acetate (EA), followed by the addition of 1-vinylimidazole (21.5 g, 0.228 mol). The mixture was stirred and refluxed at 75 °C for 24 h. After cooling, DI water was added to the resulting orange precipitate to improve flowability, followed by three extractions with EA to remove excess reactants and intermediates. Subsequently, 100 mL of DI water containing excess LiTFSI (57.8 g) was added for ion exchange and stirred for 2 h. The precipitate was

separated, washed three times with saturated sodium chloride solution, and the organic layer was purified with activated charcoal and anhydrous magnesium sulfate. The product was obtained by rotary evaporation as the IL.

2.4. Synthesis of [VIm-C12-VIm][TFSI]

[VIm-C12-VIm][TFSI] was synthesized by reacting 1,12-di-bromododecane with 1-vinylimidazole, following the same procedure as that described for [VIm-PEG$_{200}$-VIm][TFSI], except that 1,12-dibromododecane was used as the starting material in place of Br-PEG$_{200}$-Br. The synthetic route is shown in Scheme S1c.

2.5. Preparation of ASEIs

For the preparation of Im-IL/POSS ASEIs, the precursor was directly applied onto the lithium metal anode and subjected to thermal polymerization (Scheme 1). Specifically, 0.127 g (0.2 mmol) of PSS-octavinyl substituted (POSS) and 0.53 g (0.8 mmol) of [VIm-PEG$_{200}$-VIm][TFSI] were separately dissolved in 2 mL of THF. The solutions were mixed and stirred for 1 hour and then 1 wt% AIBN was added as a thermal initiator and stirred for 30 min. Subsequently, 55 μL of the precursor mixture was cast onto the lithium metal surface (diameter = 15.6 mm) and covered with a separator to absorb excess liquid. The assembly was then heated at 60 °C overnight to complete the polymerization, yielding the ASEI, denoted as VP200. Following an analogous procedure, 0.61 g (0.8 mmol) of [VIm-C12-VIm][TFSI] was employed to obtain the VC12 sample (Scheme S1).

2.6. Characterization

The chemical structures of the imidazole-based IL and Im-IL/POSS composites were confirmed by ^{1}H NMR spectroscopy (Bruker Avance 600 NMR spectrometer, solvent: d_6-DMSO). Fourier-transform infrared spectrometry (FT-IR, Thermo Nicolet Nexus 6700) was employed to identify functional groups, with spectra collected in the range of 400–4000 cm^{-1}.
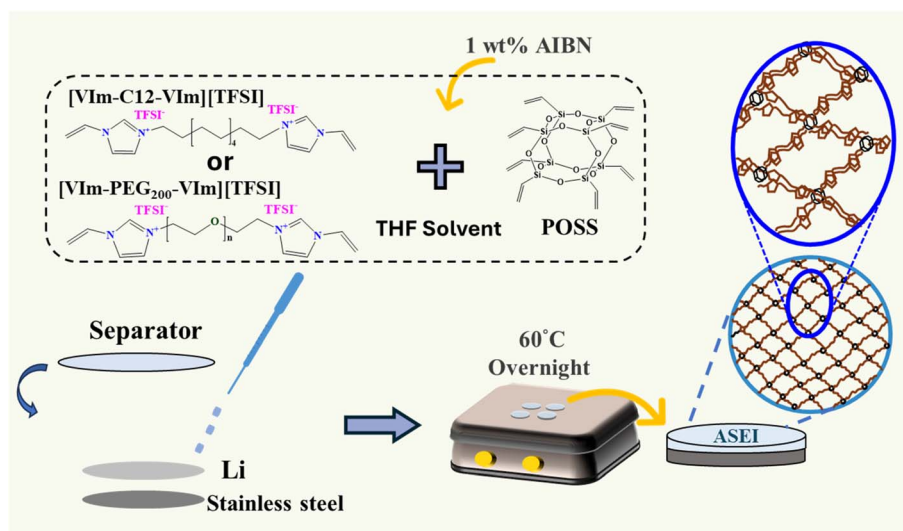
Mechanical properties were evaluated using a nanoindenter instrument (NanoIndenter G200). Cross-sectional morphology and elemental distribution were characterized by field-emission scanning electron microscopy (FE-SEM, Hitachi SU8000) coupled with energy-dispersive X-ray spectroscopy (EDS, Bruker XFlash 6I100). Post-cycling surface morphology and cross-sectional structures were examined using scanning electron microscopy (SEM, Hitachi SU-8010). X-ray photoelectron spectroscopy (XPS, PHI VersaProbe 4) analyzed the surface chemical composition of cycled lithium anodes. All the XPS samples were prepared and cut inside a glove box and then mounted to the vacuum stage with carbon tape.

2.7. Electrochemical measurements

The electrochemical stability window of the electrolyte membranes was determined by linear sweep voltammetry (LSV) using Im-IL/POSS@Li cells on an SP-300 machine at a scan rate of 5 mV s^{-1} over the potential range of 0–6 V at room temperature. Cyclic voltammetry (CV) was also performed to examine the electrochemical stability of the Im-IL/POSS ASEI using the same instrument, with a scan rate of 0.1 mV s^{-1}. The potential was swept from 0 V to 6 V (vs. Li/Li$^+$) starting at 0 V. Additionally, CV tests within the potential window of 0–4.3 V (vs. Li/Li$^+$) were conducted in the forward scan direction.

The charge–discharge performance of CR2032 coin cells with the Im-IL/POSS@Li|LFP configuration was measured at room temperature using a battery testing system (Acutech Systems, BAT-750B). Electrochemical impedance spectroscopy (EIS) measurements for Im-IL/POSS@Li|LFP cell systems were carried out on an SP-300 electrochemical workstation. The spectra were recorded at room temperature with a 5 mV AC amplitude over a frequency range of 0.1–10 MHz.

Lithium-ion transference numbers (T_{Li^+}) were determined from symmetric Li|electrolyte|Li cells according to eqn (1), where I_0 and I_s denote the initial and steady-state currents, R_0

Scheme 1 Schematic diagram of the ASEI fabrication process on the lithium metal anode.

and R_s are the interfacial resistances measured before and after polarization, and ΔV (0.01 V) is the applied potential.

$$T_{\text{Li}^+} = \frac{I_s(\Delta V - I_0 R_0)}{I_0(\Delta V - I_s R_s)} \tag{1}$$

In addition, symmetrical lithium cells were assembled to investigate lithium dendrite growth behavior, which was monitored using a NEWARE CT-4000 testing system.

3. Results and discussion

3.1. Characterization of monomers and ASEIs

3.1.1 Br-PEG$_{200}$-Br. The ^{1}H NMR spectra of the commercially available PEG$_{200}$ and the synthesized Br-PEG$_{200}$-Br are shown in Fig. S1a and b, respectively. In PEG$_{200}$, the proton resonance of the repeating ethylene glycol units appears at $\delta = 3.5$ ppm (a), while the terminal hydroxyl proton is observed at $\delta = 4.55$ ppm (d). The neighboring methylene protons (b) and (c) resonate further downfield owing to the deshielding effect of the hydroxyl substituent. After bromination, the hydroxyl proton signal at $\delta = 4.55$ ppm disappears, and the two terminal methylene signals shift from 3.4 ppm (c) and 3.47 ppm (b) to 3.57 ppm (c) and 3.73 ppm (b), respectively. Importantly, no extraneous peak corresponding to solvents or impurities is detected, confirming the successful synthesis of Br-PEG$_{200}$-Br with high purity.

3.1.2 [VIm-PEG$_{200}$-VIm][TFSI]. The ^{1}H NMR spectrum of [VIm-PEG$_{200}$-VIm][TFSI] is presented in Fig. 1a. The signals at $\delta = 2.5$ ppm and $\delta = 3.3$ ppm correspond to the solvent peaks of DMSO. The repeating ethylene glycol units give rise to a resonance peak at $\delta = 3.5$ ppm (a). In comparison, the terminal PEG protons adjacent to the imidazole substituents appear further downfield at $\delta = 3.7$ ppm (b) and $\delta = 4.3$ ppm (c). The imidazolium ring protons resonate at $\delta = 7.8$ ppm (f), $\delta = 8.1$ ppm (e), and $\delta = 9.4$ ppm (d), consistent with their deshielded environments. In addition, the three vinyl proton signals associated with the terminal groups are clearly resolved at $\delta = 5.4$ ppm (i), $\delta = 5.9$ ppm (h), and $\delta = 7.3$ ppm (g). Integration of all characteristic signals yields proton ratios that match the molecular structure, thereby supporting the successful introduction of both the imidazolium and vinyl functionalities. The absence of unexpected resonances indicates that [VIm-PEG$_{200}$-VIm][TFSI] was obtained in high purity. Further confirmation of the ion exchange process was obtained by FT-IR spectroscopy (Fig. 1c). In agreement with the reported data,[54] the [TFSI]$^-$ anion exhibits characteristic –SO$_2$ stretching bands at 1132 (symmetric S=O) and 1350 cm^{-1} (asymmetric S=O), together with a C–F$_3$ band at 1170 cm^{-1}. Comparison of the spectra before and after exchange unambiguously verifies the incorporation of [TFSI]$^-$, conforming to the successful formation of [VIm-PEG$_{200}$-VIm][TFSI].
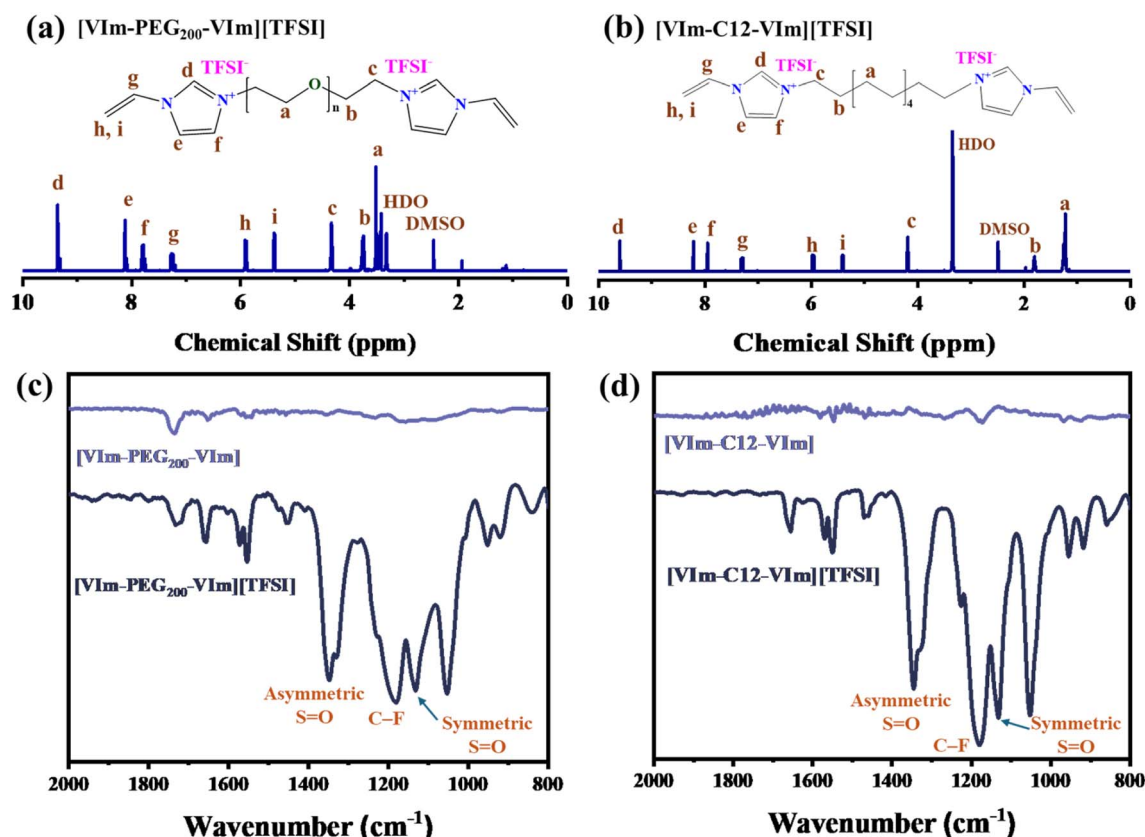

Fig. 1 (a) ^{1}H NMR spectrum of [VIm-PEG$_{200}$-VIm][TFSI] and (b) [VIm-C12-VIm][TFSI] in d_6-DMSO; (c) FT-IR spectra of [VIm-PEG$_{200}$-VIm] and [VIm-PEG$_{200}$-VIm][TFSI] and (d) [VIm-C12-VIm] and [VIm-C12-VIm][TFSI].

3.1.3 [VIm-C12-VIm][TFSI]. The ^{1}H NMR spectrum of [VIm-C12-VIm][TFSI] is shown in Fig. 1b. The signals at $\delta = 2.5$ ppm and $\delta = 3.3$ ppm correspond to the solvent peaks of DMSO. The aliphatic region is dominated by the methylene resonances of the dodecyl chain, with the main repeating $(-(CH_2)_4-)$ signal at $\delta = 1.2$ ppm (a). The terminal methylenes adjacent to the imidazolium group are observed further downfield at $\delta = 1.8$ ppm (b) and $\delta = 4.2$ ppm (c). The characteristic imidazolium ring protons resonate at $\delta = 7.9$ ppm (f), $\delta = 8.2$ ppm (e), and $\delta = 9.6$ ppm (d), while the three vinyl protons give distinct signals at $\delta = 5.4$ ppm (i), $\delta = 5.9$ ppm (h), and $\delta = 7.3$ ppm (g). Integration of the diagnostic resonances yielded proton ratios consistent with the proposed structure; for example, the integration ratio of f : c : a is 1 : 2 : 8, which is in excellent agreement with the expected values. The clean spectral profile, without additional peaks from side products or solvents, confirms that [VIm-C12-VIm][TFSI] was obtained in high purity.

FT-IR spectroscopy further corroborates the successful ionic exchange (Fig. 1d). Similar to the PEG-based analogue, the [TFSI]$^-$ anion introduces characteristic absorption in the 1100–1400 cm^{-1} region, specifically the symmetric and asymmetric –SO$_2$ stretching bands at 1132 and 1350 cm^{-1}, together with a C–F$_3$ vibration at 1170 cm^{-1}.[54] The emergence of these bands, accompanied by the disappearance of precursor-related features, provides clear evidence of complete ion exchange and confirms the formation of [VIm-C12-VIm][TFSI].

3.2. Properties of the ASEI

The FT-IR spectra of the ASEI layers (VC12 and VP200) and the ILs ([VIm-C12-VIm][TFSI] and [VIm-PEG$_{200}$-VIm][TFSI]) in the range of 1700–1600 cm^{-1} show a characteristic C=C stretching band at around 1655 cm^{-1} for the vinyl groups in the imidazole ILs, which completely disappears after the POSS reaction (Fig. S2), confirming full vinyl consumption and successful PIL–POSS crosslinking. Scheme S2 illustrates the PIL–POSS ASEI's novelty. The crosslinked imidazolium network selectively conducts Li$^+$ while repelling anions (TFSI$^-$/PF$_6^-$/NO$_3^-$), creating uniform Li$^+$ flux, while robust POSS cages maintain conformal contact during volume changes to prevent dendrite penetration.

The nanoindentation test results for VC12 and VP200 ASEI layers are shown in Fig. S3. The load–displacement curves (Fig. S3a and b) show the raw response of applied load (mN) *versus* indentation depth (nm), both exhibiting the expected nonlinear increase with depth. VC12 (a) displays a steeper initial slope than VP200 (b), indicating higher resistance to penetration and greater stiffness. Hardness as a function of indentation depth (Fig. S3c and d) reveals that VC12 reaches a maximum hardness of 6.8 GPa at shallow depths, followed by a gradual decrease attributed to substrate effects. In contrast, VP200 (d) exhibits a lower maximum hardness of 5.1 GPa with a flatter profile, confirming its softer mechanical nature. The fluctuations observed in the VC12 curve may arise from surface heterogeneity or stronger interfacial interactions with the stainless-steel substrate. This ~33% hardness disparity stems from the VC12 linear C12 alkyl spacer, which promotes dense chain packing and robust π–π stacking among rigid imidazole rings,[55,56] whereas the VP200 flexible PEG$_{200}$ linker introduces steric hindrance and chain entanglement and reduced interchain interactions,[57] yielding a softer profile optimal for high-rate applications. Cross-sectional SEM images (Fig. S4a and g) and EDS elemental mapping (Fig. S4b–f for VC12; Fig. S4h–l for VP200) confirmed the homogeneous organic–inorganic hybrid structure. Uniform C, O, Si, and N distribution throughout both ASEI layers verifies well-dispersed POSS (Si signal) and imidazolium (N signal) components without phase segregation, ensuring consistent Li$^+$ transport pathways and mechanical integrity.

3.3. Electrochemical performance of the modified Li anode

Fig. 2a presents the LSV curves for untreated lithium metal (bare Li) and lithium metal coated with Im-IL/POSS composites (VC12@Li and VP200@Li). Bare Li exhibits a current onset at around 4 V, whereas both VC12@Li and VP200@Li remain stable up to approximately 5 V. This enhanced stability can be attributed to the presence of the TFSI anion in the IL, which broadens the electrochemical window and confirms the excellent electrochemical stability of the ASEI. Following the LSV results, cyclic voltammetry (CV) tests were performed to identify potential reactions based on oxidation and reduction peaks, as shown in Fig. 2b. Bare Li exhibits pronounced current responses, indicative of unstable interfacial reactions. By comparison, VC12@Li and VP200@Li display suppressed current densities, reflecting enhanced interfacial stability.
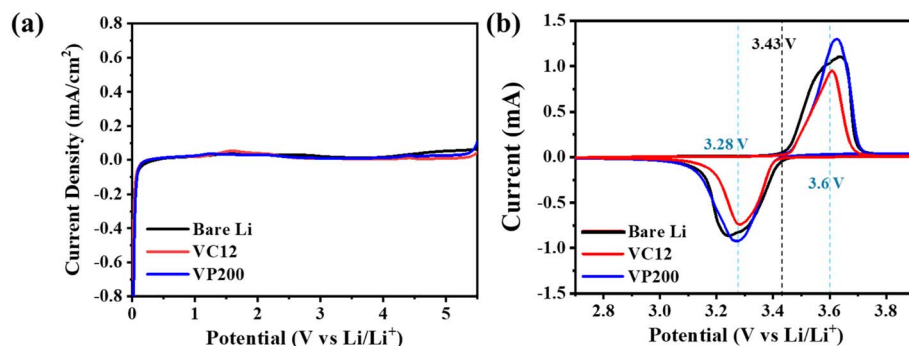

Fig. 2 (a) LSV curves recorded within 0–6 V; (b) CV curves of untreated lithium metal (bare Li), VC12@Li, and VP200@Li.
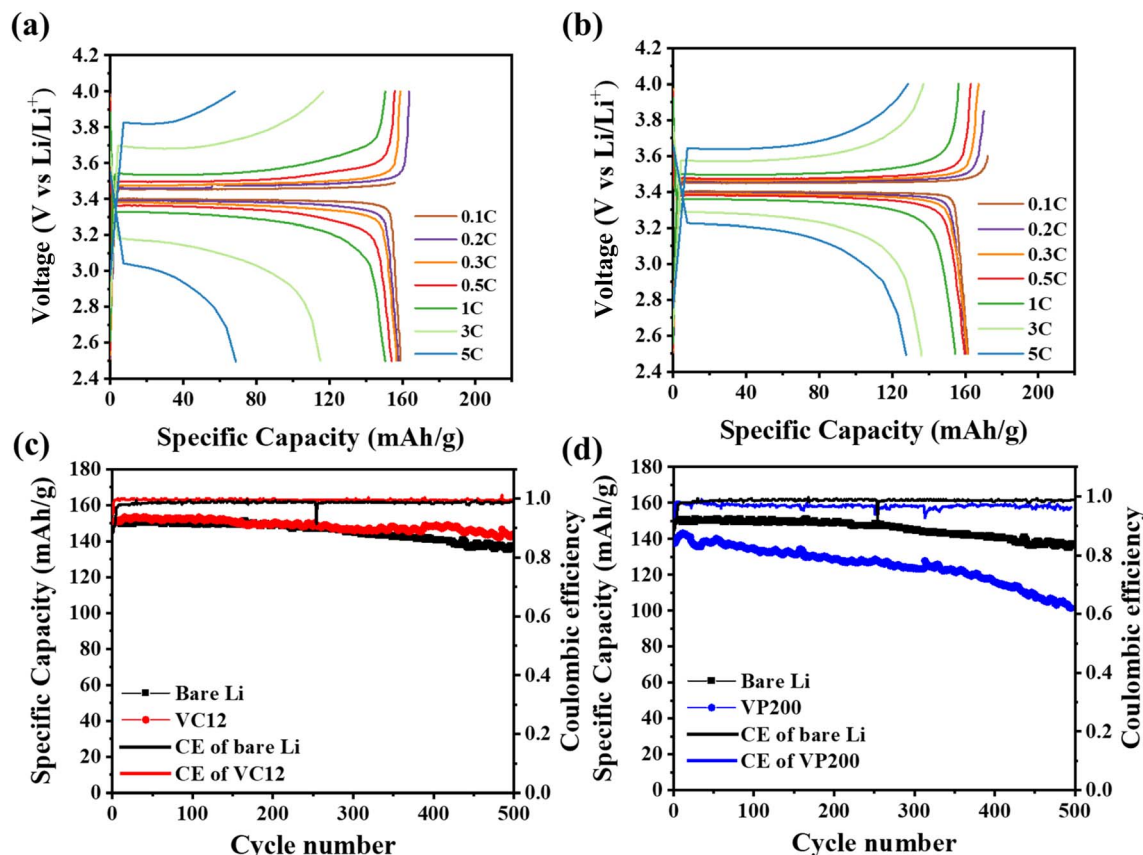
Fig. 3 Charge–discharge curves of (a) VC12@Li|LFP and (b) VP200@Li|LFP cells; (c) cycling performance of VC12@Li|LFP and (d) VP200@Li|LFP cells compared with Li|LFP cells.

VC12@Li shows more defined and stable features than VP200@Li, suggesting superior electrochemical reversibility. A distinct current signal appears at 3.43 V, corresponding to the operating potential of LFP, while peaks at 3.6 V and 3.28 V can be assigned to lithium-ion intercalation and deintercalation, respectively. The absence of additional current signals confirms the electrochemical stability of the ASEI. Reversibility was further assessed by analyzing the anodic ($I_{p,a}$) and cathodic ($I_{p,c}$) peak potentials and by calculating the charge (Q) from the CV curves using the formula: $Q = (i \times E)/\nu$, where $i \times E$ represents the integrated peak area and ν is the scan rate. The resulting charge ratios (Q_a/Q_c), summarized in Table S1, are close to unity for both systems, confirming stable and nearly reversible electrochemical reactions. Notably, the peak current ratio of VC12@Li (1.27) is lower than that of VP200@Li (1.4), indicating more reversible ion diffusion and reaction kinetics in VC12@Li.

The electrochemical performance of the Im-IL/POSS@Li|LFP cells was evaluated by charge–discharge testing. Following activation at 0.1C for three cycles to establish a stable SEI layer, the cells were cycled at various C-rates within a voltage window of 2.5–4.0 V at 25 °C. As shown in Fig. 3a and b (with Li|LFP cells for comparison provided in Fig. S4a), both ASEI-containing cells (VC12 and VP200) delivered higher capacities than bare Li at elevated current densities, confirming that the ASEI effectively suppresses parasitic reactions, stabilizes the Li interface, and

mitigates dendrite growth. Between the two ASEI materials, VP200 exhibited a slightly higher rate capacity, with discharge capacities of 122.2 and 89.4 mAh g^{-1} at 3C and 5C, respectively, compared to 116.7 and 68.8 mAh g^{-1} for VC12. This enhancement may be attributed to the PEG segments in VP200, which facilitate Li$^+$ transport and support improved high-rate performance. Nevertheless, VC12 demonstrated superior cycling stability, as reflected in coulombic efficiency and long-term cycling performance at 1C, retaining 94.7% capacity after 500 cycles (*vs.* 90.7% for bare Li and 72.9% for VP200@Li|LFP; Fig. 3c and d) and 84.6% capacity after 1000 cycles (Fig. S4b). These findings highlight that while VP200 favors Li$^+$ transport at high rates, VC12 provides a more stable interphase, thereby extending cell lifespan.

The EIS results for bare Li, VC12, and VP200 are presented in Fig. S5c and 4a, b. The Nyquist plots display a semicircular arc followed by a straight line, with the arc composed of two overlapping semicircles corresponding to the solid electrolyte interphase resistance (R_{SEI}) and charge-transfer resistance (R_{ct}). For fitting, the equivalent circuit was used to fit data in Fig. S5d, and the spectral results were deconvoluted into bulk resistance (R_b), R_{SEI}, and R_{ct}, and the extracted values are summarized in Table S2. The bulk impedance (R_b), attributed to internal cell materials and assembly, remained essentially constant throughout cycling. The R_{SEI}, associated with the first
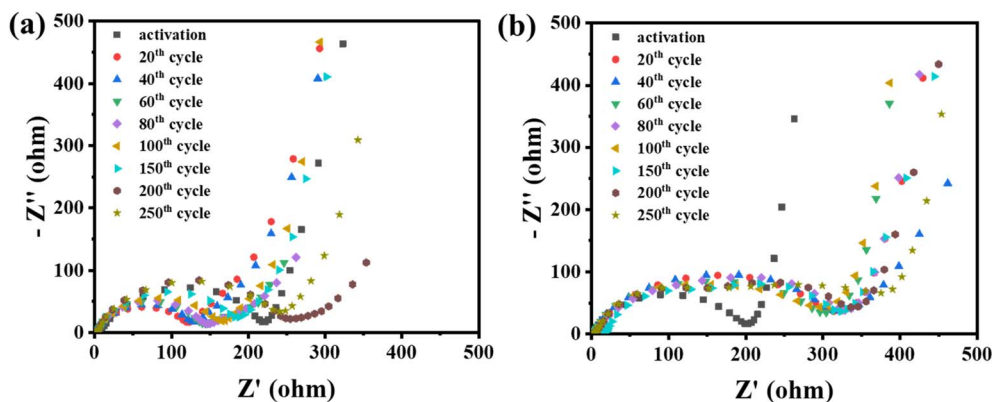
Fig. 4 (a) EIS profiles of VC12@Li|LFP cells and (b) VP200@Li|LFP cells.

semicircle, originates from the SEI layer at the electrode–electrolyte interface. Its gradual increase during cycling is attributed to lithium dendrite growth. Among the samples, VC12 exhibited the lowest R_{SEI}, indicating more uniform dendrite suppression, while VP200 showed intermediate values higher than that of VC12 but lower than that of bare Li, consistent with enhanced Li$^+$ transport facilitated by POSS. The R_{ct}, represented by the second semicircle, reflects interfacial charge-transfer kinetics. VC12 maintained the lowest R_{ct} during the first 200 cycles, after which it increased, likely due to SEI thickening and the formation of the cathode–electrolyte interface (CEI).[58] VP200 displayed slightly lower R_{ct} than bare Li, confirming its improved ionic conduction across the ASEI.

Lithium-ion transference numbers were determined for symmetric VC12@Li and VP200@Li cells using the Bruce–Vincent method (Table S3 and Fig. S6a, b), yielding T_{Li^+} values of 0.62 and 0.59, respectively. These values are markedly higher than typical reports for 1 M LiPF$_6$ in EC/DEC (1 : 1, v/v), where T_{Li^+} generally lies in the range 0.3–0.4 (e.g., T_{Li^+} = 0.29 (ref. 59) and 0.38 (ref. 60)). This enhanced Li$^+$ contribution is consistent with efficient Li$^+$ transport across the artificial interphase, as expected for optimized battery electrolytes. The slightly higher

T_{Li^+} of VC12 correlates with its lower interfacial resistances (R_{SEI} and R_{ct}) extracted from EIS, supporting the conclusion that VC12 forms a more Li$^+$-conductive and stable interphase than VP200, in line with its superior long-term impedance and cycling performance.

Lithium symmetric cells were further assembled to evaluate dendrite growth (Fig. S7a). When cycled at increasing current densities (0.1–3.0 mA cm^{-2}), the bare Li cell exhibited large voltage fluctuations, rapid polarization growth, and unstable cycling, indicative of severe dendrite growth and unstable interfacial reactions. In contrast, the VC12@Li cell maintains a relatively smooth and stable voltage profile with significantly lower overpotentials, even at higher current densities. This demonstrates that the ASEI formed by VC12 effectively suppresses lithium dendrite penetration, stabilizes the Li surface, and ensures prolonged cycling stability compared to bare Li. Long-term stability tests (Fig. S7b) further demonstrate VC12@Li's superior endurance after 800 hours at 0.5 mA cm^{-2} with stable overpotentials, confirming ASEI's mechanical robustness and effective dendrite suppression under prolonged Li plating/stripping. These results collectively validate the
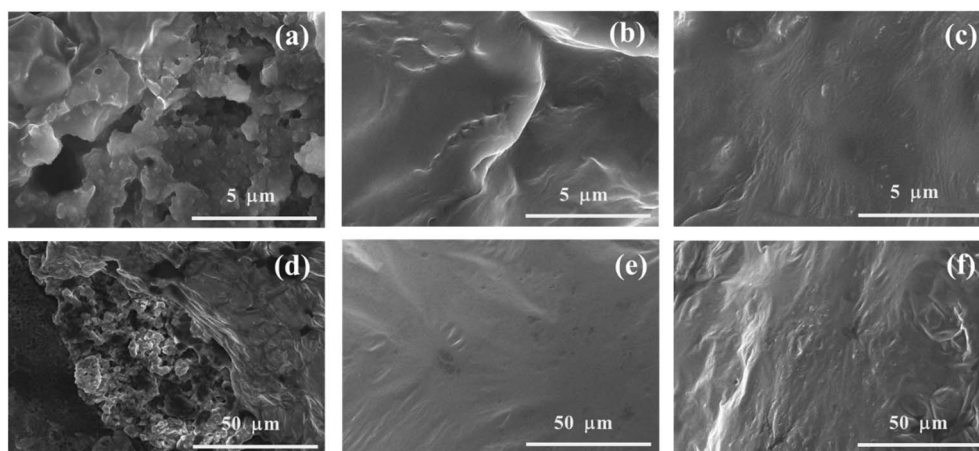

Fig. 5 SEM images of (a and d) bare Li, (b and e) VC12@Li, and (c and f) VP200@Li. The Li|LFP, VC12@Li|LFP, and VP200@Li|LFP cells were disassembled after 100 cycles at 1C.
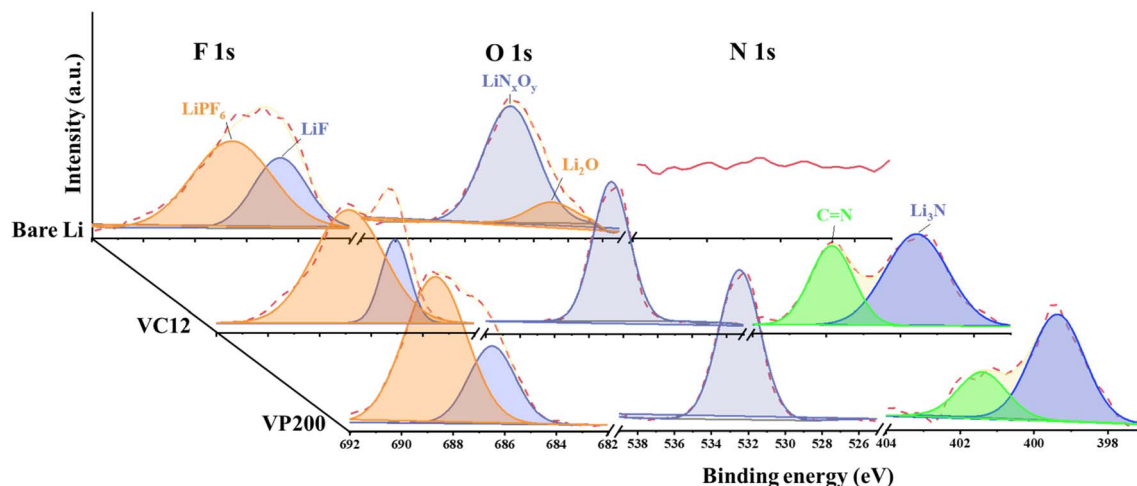
Fig. 6 F 1s, O 1s and N 1s XPS spectra of bare Li, VC12@Li, and VP200@Li using 1 M LiPF$_6$ in EC/DEC (1 : 1, v/v). The Li|LFP, VC12@Li|LFP, and VP200@Li|LFP cells were disassembled after 100 cycles at 1C.

ability of the PIL–POSS ASEI's layer to stabilize the Li interface across diverse cycling conditions.

3.4. Internal analysis of the battery after cycling

To evaluate the ASEI layers formed on the lithium-metal anodes, cross-sectional SEM was used to measure their thickness. Controlling this thickness is essential, since overly thick coatings hinder Li$^+$ transport and degrade performance. As shown in Fig. S8, VC12@Li forms a uniform ASEI layer of about 7 μm, conformally covering the lithium surface. Building on previous results demonstrating that the Im/IL/POSS ASEI lowers impedance and improves cycling, we further examined its stability under practical conditions. Cells were cycled 100 times at 1C (2.5–4 V) and then disassembled in a glove box for post-mortem SEM and XPS analyses. The SEM images of bare Li, VC12@Li, and VP200@Li highlight clear differences in surface morphology (Fig. 5). Bare Li shows irregular dendrites on the Li surface (Fig. 5a and d), while VC12@Li (Fig. 5b and e) maintains a smooth and compact surface, showing strong dendrite suppression. VP200@Li produced a smoother surface than bare Li (Fig. 5c and f), but it was less uniform than VC12@Li. Overall,

Im-IL/POSS ASEIs promote more uniform Li deposition, with the VC12 ASEI providing the most effective protection.

XPS spectra of bare Li, VC12@Li, and VP200@Li electrodes were collected after cycling to analyze the near-surface chemical composition of the interphase (Fig. 6 and S9). The C 1s spectra show C–C, C=C, and C–H signals appearing at 284–285 eV in all samples (Fig. S9), originating mainly from the materials, electrolyte, and Super P in the cathode. The peak at around 286 eV corresponds to C–N, C=N, and C–O bonds, while those near 290 eV are assigned to C=N$^+$ and C=O species and decomposition products such as Li$_2$CO$_3$, RO–CO$_2$Li, and (CH$_2$OCO$_2$Li)$_2$ formed during cycling. The F 1s spectra reveal LiF at 685–686 eV (Fig. 6), a key SEI component providing stability, and LiPF$_6$ at 687–688 eV. Notably, the relative LiPF$_6$ contribution is higher for VC12 (77.3%) and VP200 (71.5%) than for bare Li (64.9%), suggesting that the Im-IL/POSS-derived ASEI suppresses LiPF$_6$ decomposition in the electrolyte.[61]

The N 1s spectra show a peak at ∼399 eV corresponding to Li$_3$N (Fig. 6), which enhances Li$^+$ conductivity, observed in both VC12@Li and VP200@Li electrodes but absent in bare Li. A signal at 401 eV is attributed to C=N groups from the coating
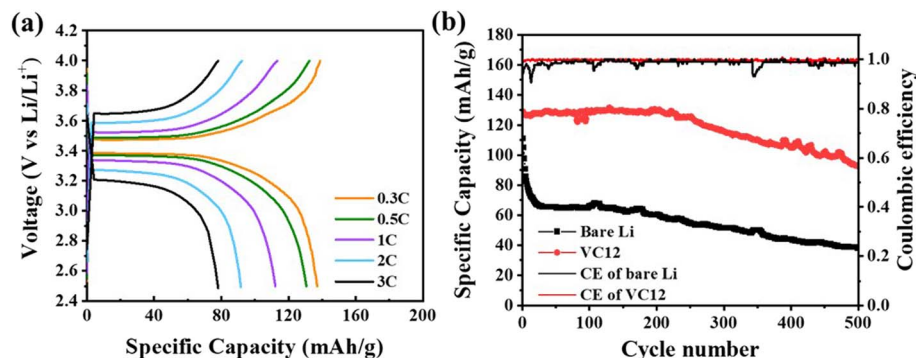

Fig. 7 (a) Charge–discharge curves of the VC12@Li|LFP cell and (b) cycling performance of the VC12@Li|LFP cell compared with that of the Li|LFP cell in 1 M LiTFSI in DOL/DME (1 : 1, v/v) containing 2 wt% LiNO$_3$.
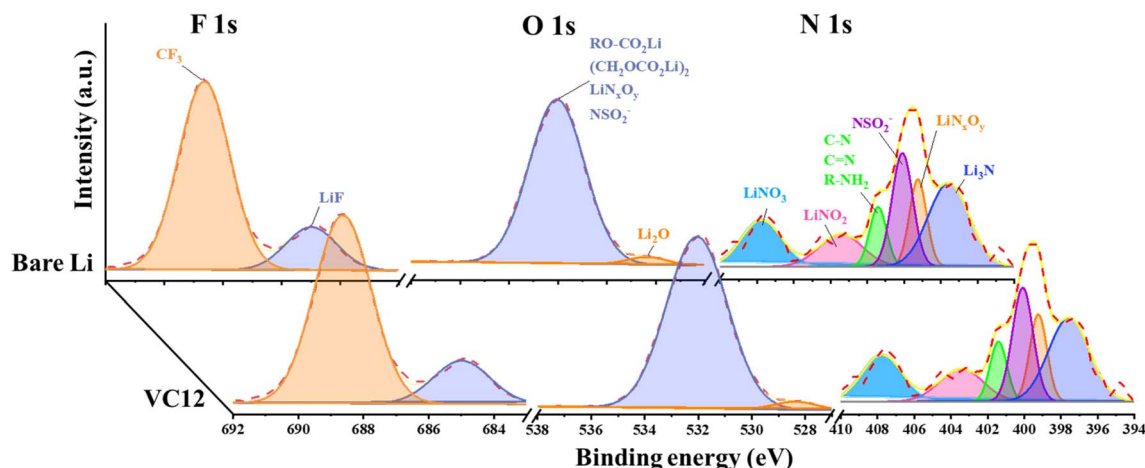
Fig. 8 F 1s, O 1s, and N 1s XPS spectra of bare Li and VC12@Li using 1 M LiTFSI in DOL/DME (1 : 1, v/v) containing 2 wt% LiNO$_3$. The Li|LFP and VC12@Li|LFP cells were disassembled after 100 cycles at 1C.

material. These findings confirm that the ASEI facilitates ion transport. The O 1s spectra provide further insights (Fig. 6). A peak at 528 eV, assigned to Li$_2$O from lithium salt oxidation, is absent in both VC12@Li and VP200@Li, supporting the protective effect of the ASEI against electrolyte decomposition. A peak near 532 eV may correspond to LiN$_x$O$_y$, which can generate Li$_3$N during cycling.[61] In contrast, bare Li presented a dominant peak at 531 eV, primarily attributed to Li$_2$CO$_3$, RO–CO$_2$Li, and (CH$_2$OCO$_2$Li)$_2$ from electrolyte degradation. Finally, the Li 1s spectra exhibit overlapping signals from Li$_3$N, Li$_2$O, LiF, and LiPF$_6$ between 55 and 56 eV (Fig. S9), complicating peak deconvolution. Nevertheless, the spectral features are consistent with the compositional assignments derived from C 1s, F 1s, N 1s, and O 1s analyses. We note that, due to the ~7 μm thickness of the ASEI and the surface sensitivity of XPS, these data primarily probe the outermost interfacial region, but they still provide qualitative evidence that the Im-IL/POSS layer promotes a LiF/Li$_3$N-rich, decomposition-suppressing surface consistent with the improved electrochemical performance.

3.5. Electrochemical performance of the modified Li anode with ether-based electrolyte

The charge–discharge profiles of Li|LFP and VC12@Li|LFP cells using ether-based electrolyte (1 M LiTFSI in DOL/DME (1 : 1, v/v) containing 2 wt% LiNO$_3$) reveal a marked difference in cycling stability (Fig. S10 and 7a). The Li|LFP cell exhibits pronounced polarization and distorted curves upon cycling, reflecting unstable SEI formation and uneven Li deposition. In contrast, the VC12@Li|LFP cell delivers highly overlapping voltage profiles with reduced overpotentials, indicating uniform Li plating/stripping and suppressed dendrite growth. These results confirm that the VC12-derived ASEI effectively stabilized the Li anode and enhanced reversibility in ether-based electrolytes. The cycling performance of the VC12@Li|LFP cell at a 1C charge–discharge rate using ether-based electrolyte showed marked improvement as compared to its Li|LFP counterpart (Fig. 7b). The Li|LFP cell exhibited rapid capacity decay,

dropping below 70 mAh g^{-1} within 100 cycles and continuing to fade to below 40 mAh g^{-1} after 500 cycles. In contrast, VC12@Li|LFP maintained stable operation with nearly 130 mAh g^{-1} after 200 cycles with 99.6% capacity retention, compared to only 46.2% for its Li|LFP counterpart. Even after 500 cycles, VC12@Li|LFP preserved 70.8% of its initial capacity, approximately 2.5 times higher than that of bare Li, highlighting the superior cycling stability imparted by the VC12 ASEI layer.

To investigate the near-surface interfacial chemistry of the ether-based electrolyte system, XPS analysis was performed on the cycled anodes (Fig. 8 and S11). The C 1s spectra (Fig. S11) exhibit characteristic peaks at 284–285 eV (C–C, C=C, and C–H), attributed to residual carbon frameworks or polymeric species, indicative of carbonized polymers within the SEI. A peak at ~286 eV is assigned to C–O species originating from solvent decomposition or the reaction with the lithium salt. The signals at ~289, 290, and 292–293 eV correspond to RO–CO$_2$Li, C=O, and C–F bonds, respectively. Compared with bare Li, the VC12-modified electrode presents reduced C=O and decomposition products but an enrichment of RO–CO$_2$Li and polymeric organic species, which are recognized to facilitate Li$^+$ transport and improve SEI stability.

The O 1s spectra reveal a pronounced Li$_2$O peak (528–529 eV) on bare Li (Fig. 8), indicating parasitic reduction and resistive inorganic byproducts. In contrast, the VC12-modified electrode suppresses Li$_2$O accumulation while promoting the formation of stable oxygenated compounds such as RO–CO$_2$Li, (CH$_2$OCO$_2$Li)$_2$, LiN$_x$O$_y$, and NSO$_2^-$ at 531–532 eV. The N 1s spectra further reveal that VC12 modification induces a higher fraction of LiN$_x$O$_y$ (~399.5 eV) (Fig. 8), beneficial for Li$^+$ conduction and interfacial passivation, while concurrently reducing unstable intermediates such as LiNO$_2$ (~404 eV). Moreover, organic nitrogen species (C–N, C=N, and R–NH$_2$, ~400.7 eV) are more abundant in the VC12-modified electrode, suggesting the presence of a flexible polymeric nitrogen-containing SEI that can accommodate electrode volume fluctuations. Residual

$LiNO_3$ ($\sim$407 eV) is also detected, serving as a potential reservoir for SEI repair and stabilization during cycling.

The F 1s spectra show contributions from LiF and $-CF_3$ groups originating from LiTFSI decomposition in both samples (Fig. 8). Notably, the VC12-modified electrode demonstrates stronger LiF formation, a favorable SEI component that enhances interfacial robustness and suppresses dendrite growth. Finally, the Li 1s spectra (Fig. S11) highlight clear contrasts: bare Li has a higher contribution from Li–O species (Li_2O and LiO_2), which raises interfacial resistance, whereas VC12 significantly increases beneficial inorganic/organic SEI components, including LiF, Li_3N, LiN_xO_y, and $RO-CO_2Li$. We note that, due to the $\sim$7 μm ASEI thickness and XPS surface sensitivity, these data primarily probe the outermost interfacial region but provide qualitative evidence of a $LiF/Li_3N/LiN_xO_y$-rich surface composition consistent with the enhanced electrochemical performance. Collectively, these results demonstrate that the VC12-modified electrode forms a more balanced SEI of stable inorganic species and flexible organics, effectively mitigating parasitic reactions and improving cycling stability.

Comparative electrochemical performance of the PIL–POSS ASEI against state-of-the-art artificial SEI (ASEI) strategies for Li metal anodes is given in Table S4. The PIL–POSS ASEI achieves a superior capacity retention of 84.6% after 1000 cycles (carbonate electrolyte) and 70.8% after 500 cycles (ether electrolyte), outperforming other ASEI layers. This exceptional stability arises from POSS cages providing mechanical reinforcement (preventing rupture during Li volume expansion) and PIL components enabling selective Li^+ conduction, minimizing dead Li formation and interfacial instability that limit conventional Li metal batteries.

4. Conclusion

In this work, we report a simple polymerization strategy to construct ASEIs on lithium metal anodes by integrating PILs with POSS. The hybrid ASEI combines the mechanical robustness of POSS with the flexibility and ionic conductivity of imidazolium-based ILs, forming a conformal crosslinked PIL–POSS network that accommodates volume changes during Li plating/stripping while effectively suppressing dendrite growth and side reactions. FT-IR and ^{1}H NMR analyses confirmed successful IL incorporation and complete PIL–POSS crosslinking. Both Im-IL/POSS@Li|LFP cells delivered higher capacities than bare Li at different C-rates. Rate capability tests further showed that the PEG-based VP200 ASEI facilitated Li^+ transport for high-rate performance, whereas dodecane-based VC12 offered superior long-term stability. VC12@Li|LFP cells retained 94.7% capacity after 500 cycles and 84.6% after 1000 cycles in carbonate-based electrolytes and 99.6% after 200 cycles in ether-based electrolytes, while maintaining 70.8% after 500 cycles—approximately 2.5 times higher than bare Li. LSV and CV confirmed a broadened electrochemical stability window of $\sim$5 V compared with $\sim$4 V for bare Li. Post-mortem analyses confirmed the ASEI's protective function, revealing smooth, compact Li deposits and a balanced SEI composition

enriched with stable inorganic species (LiF, Li_3N, and LiN_xO_y) and flexible organic moieties ($RO-CO_2Li$ and polymeric nitrogen species). These components enhanced Li^+ mobility, inhibited electrolyte decomposition, and minimized resistive Li_2O formation. Overall, the PIL–POSS hybrid ASEI provides a practical route to dense, conductive, and mechanically robust interphases, enabling safer and longer-lasting lithium metal batteries.

Conflicts of interest

The authors declare that they have no known competing financial interests or personal relationships that could have appeared to influence the work reported in this paper.

Author contributions

Wei-Ting Chou: conceptualization, formal analysis, investigation, writing – original draft. Thi-Ngoc Pham: data curation, investigation, validation, writing – original draft. Ta-Ching Yang: formal analysis, investigation, data curation. Yun-Jie Tsai: investigation, validation. Hsisheng Teng: validation, funding acquisition, writing – review & editing. Jeng-Shiung Jan: conceptualization, supervision, funding acquisition, project administration, writing – review & editing.

Data availability

The data supporting this article have been included as part of the supplementary information (SI). Supplementary information: the experimental part and other necessary data. See DOI: https://doi.org/10.1039/d5ta07774e.

Acknowledgements

References

1 E. Peled, *J. Electrochem. Soc.*, 1979, **126**, 2047.
2 D. Aurbach, M. Daroux, P. Faguy and E. Yeager, *J. Electrochem. Soc.*, 1987, **134**, 1611.
3 E. Peled, D. Golodnitsky and G. Ardel, *J. Electrochem. Soc.*, 1997, **144**, L208.
4 D. Aurbach, B. Markovsky, M. Levi, E. Levi, A. Schechter, M. Moshkovich and Y. Cohen, *J. Power Sources*, 1999, **81**, 95–111.

5 A. v. Cresce, S. M. Russell, D. R. Baker, K. J. Gaskell and K. Xu, *Nano Lett.*, 2014, **14**, 1405–1412.

6 Y. Wang, S. Nakamura, M. Ue and P. B. Balbuena, *J. Am. Chem. Soc.*, 2001, **123**, 11708–11718.

7 Z. Chen, G. Xu, J. Jiang, Q. Wu, S. Liu, Y. Feng, Y. Li, L. Zhang and X. Sun, *J. Power Sources*, 2024, **602**, 234311.

8 W. Xu, X. Liao, W. Xu, C. Sun, K. Zhao, Y. Zhao and C. Hu, *Nano Energy*, 2021, **88**, 106237.

9 X. Q. Zhang, X. B. Cheng, X. Chen, C. Yan and Q. Zhang, *Adv. Funct. Mater.*, 2017, **27**, 1605989.

10 H. Zhang, C. Shen, Y. Huang and Z. Liu, *Appl. Surf. Sci.*, 2021, **537**, 147983.

11 H. Zhu, M. H. A. Shiraz, L. Liu, Y. Hu and J. Liu, *Nanotechnology*, 2021, **32**, 144001.

12 C. Yu, X. Chen, Z. Xiao, C. Lei, C. Zhang, X. Lin, B. Shen, R. Zhang and F. Wei, *Nano Lett.*, 2019, **19**, 5124–5132.

13 J. Li, N. J. Dudney, J. Nanda and C. Liang, *ACS Appl. Mater. Interfaces*, 2014, **6**, 10083–10088.

14 Z. Lin, Y. Ma, W. Wang, Y. He, M. Wang, J. Tang, C. Fan and K. Sun, *J. Energy Chem.*, 2023, **76**, 631–638.

15 D. Kang, S. Sardar, R. Zhang, H. Noam, J. Chen, L. Ma, W. Liang, C. Shi and J. P. Lemmon, *Energy Storage Mater.*, 2020, **27**, 69–77.

16 L. Fan, Z. Guo, Y. Zhang, X. Wu, C. Zhao, X. Sun, G. Yang, Y. Feng and N. Zhang, *J. Mater. Chem. A*, 2020, **8**, 251–258.

17 I. H. Son, J. H. Park, S. Kwon, J. Mun and J. W. Choi, *Chem. Mater.*, 2015, **27**, 7370–7379.

18 D. A. Dalla Corte, A. C. Gouget-Laemmel, K. Lahlil, G. Caillon, C. Jordy, J.-N. Chazalviel, T. Gacoin, M. Rosso and F. Ozanam, *Electrochim. Acta*, 2016, **201**, 70–77.

19 H.-Y. Wang and F.-M. Wang, *J. Power Sources*, 2013, **233**, 1–5.

20 Y. Zhao, M. Amirmaleki, Q. Sun, C. Zhao, A. Codirenzi, L. V. Goncharova, C. Wang, K. Adair, X. Li and X. Yang, *Matter*, 2019, **1**, 1215–1231.

21 W. Xiong, T. Huang, Y. Feng, X. Ye, X. Li, J. Liang, S. Ye, X. Ren, Y. Li, Q. Zhang and J. Liu, *J. Mater. Chem. A*, 2021, **9**, 18338–18348.

22 E. Kianfar and S. Mafi, *Fine Chem. Eng.*, 2021, 21–29.

23 B. M. Quinn, Z. Ding, R. Moulton and A. J. Bard, *Langmuir*, 2002, **18**, 1734–1742.

24 T. Li and W. Hu, *Green Energy Environ.*, 2024, **9**, 604–622.

25 D. R. MacFarlane, M. Forsyth, P. C. Howlett, J. M. Pringle, J. Sun, G. Annat, W. Neil and E. I. Izgorodina, *Acc. Chem. Res.*, 2007, **40**, 1165–1173.

26 T. Zhou, X. Gao, B. Dong, N. Sun and L. Zheng, *J. Mater. Chem. A*, 2016, **4**, 1112–1118.

27 D. Shang, J. Fu, Q. Lu, L. Chen, J. Yin, X. Dong, Y. Xu, R. Jia, S. Yuan and Y. Chen, *Solid State Ionics*, 2018, **319**, 247–255.

28 J.-K. Kim, A. Matic, J.-H. Ahn and P. Jacobsson, *J. Power Sources*, 2010, **195**, 7639–7643.

29 T. Sugimoto, Y. Atsumi, M. Kikuta, E. Ishiko, M. Kono and M. Ishikawa, *J. Power Sources*, 2009, **189**, 802–805.

30 H. Sun, G. Zhu, Y. Zhu, M. C. Lin, H. Chen, Y. Y. Li, W. H. Hung, B. Zhou, X. Wang and Y. Bai, *Adv. Mater.*, 2020, **32**, 2001741.

31 M. Deyab, *J. Power Sources*, 2018, **390**, 176–180.

32 K. Chatterjee, A. D. Pathak, A. Lakma, C. S. Sharma, K. K. Sahu and A. K. Singh, *Sci. Rep.*, 2020, **10**, 9606.

33 T. H. Wang, C. Chen, N. W. Li, K. Su, X. Wu, L. Yu and X. C. Chen, *Chem. Eng. J.*, 2022, **439**, 135780.

34 Y.-C. Tseng, S.-H. Hsiang, C.-H. Tsao, H. Teng, S.-S. Hou and J.-S. Jan, *J. Mater. Chem. A*, 2021, **9**, 5796–5806.

35 Y.-C. Tseng, S.-H. Hsiang, T.-Y. Lee, H. Teng, J.-S. Jan and T. Kyu, *ACS Appl. Energy Mater.*, 2021, **4**, 14309–14322.

36 Y.-C. Tseng, F. I. Ramdhani, S.-H. Hsiang, T.-Y. Lee, H. Teng and J.-S. Jan, *J. Membr. Sci.*, 2022, **641**, 119891.

37 T. He, Y. Han, B. Shi, J. Wang and H. Yang, *J. Mater. Chem. A*, 2024, **12**, 32593–32612.

38 N. Maleki, A. Safavi and F. Tajabadi, *Anal. Chem.*, 2006, **78**, 3820–3826.

39 F. Zhang, Z. Wang, L. Wang, W. Li, A. Pan, H. Song, J. Xu, J. Hu and X. Wu, *Chem. Eng. J.*, 2022, **435**, 135101.

40 X. Zhang, L. Su, F. Lu, Y. Tian, F. Xie, L. Liang, L. Zheng and X. Gao, *Green Chem.*, 2023, **25**, 8759–8769.

41 J. Wellmann, J.-P. Brinkmann, B. r. Wankmiller, K. Neuhaus, U. Rodehorst, M. R. Hansen, M. Winter and E. Paillard, *ACS Appl. Mater. Interfaces*, 2021, **13**, 34227–34237.

42 S. Wang, L. Tan, C. Zhang, I. Hussain and B. Tan, *J. Mater. Chem. A*, 2015, **3**, 6542–6548.

43 D. P. Shang, J. F. Fu, Q. Lu, L. Y. Chen, J. T. Yin, X. Dong, Y. F. Xu, R. R. Jia, S. Yuan, Y. Chen and W. Deng, *Solid State Ionics*, 2018, **319**, 247–255.

44 Q. Lu, J. Fu, L. Chen, D. Shang, M. Li, Y. Xu, R. Jia, S. Yuan and L. Shi, *J. Power Sources*, 2019, **414**, 31–40.

45 Y. Liu, Y. Huang and L. Liu, *Compos. Sci. Technol.*, 2007, **67**, 2864–2876.

46 M. Longhi, L. P. Zini, V. Pistor, S. R. Kunst and A. J. Zattera, *Mater. Res.*, 2017, **20**, 1388–1401.

47 X. Song, Z. Wang, F. Zhao, Y. Sun, B. Cheng and J. Xing, *Adv. Mater. Interfaces*, 2021, **8**, 2100458.

48 A. Omrani, H. Rostami and R. Minaee, *Prog. Org. Coat.*, 2016, **90**, 331–338.

49 C. C. Chang, M. H. Shen, Y. S. Hsu, H. Teng and J. S. Jan, *Small Sci.*, 2024, **4**, 2400183.

50 G. Yang, C. Chanthad, H. Oh, I. A. Ayhan and Q. Wang, *J. Mater. Chem. A*, 2017, **5**, 18012–18019.

51 Y. Shin, A. Le Mong, C. Nguyen Thi Linh and D. Kim, *J. Mater. Chem. A*, 2024, **12**, 13980–13993.

52 Y.-T. Weng, H.-W. Liu, A. Pei, F. Shi, H. Wang, C.-Y. Lin, S.-S. Huang, L.-Y. Su, J.-P. Hsu and C.-C. Fang, *Nat. Commun.*, 2019, **10**, 5824.

53 P. Liu, J. Zhang, L. Zhong, S. Huang, L. Gong, D. Han, S. Wang, M. Xiao and Y. Meng, *Small*, 2021, **17**, 2102454.

54 A. P. Martins, A. Fdz De Añastro, J. L. Olmedo-Martínez, A. R. Nabais, L. A. Neves, D. Mecerreyes and L. C. Tomé, *Membranes*, 2020, **10**, 46.

55 Y. L. Wang, A. Laaksonen and M. D. Fayer, *J. Phys. Chem. B*, 2017, **121**, 7173–7179.

56 F. Tang, T. Ohto, T. Hasegawa, M. Bonn and Y. Nagata, *Phys. Chem. Chem. Phys.*, 2017, **19**, 2850–2856.

57 M. Nishida, T. Tanaka, T. Miki, I. Shigematsu and K. Kanayama, *RSC Adv.*, 2019, **9**, 15657–15667.

58 S. P. Kühn, K. Edström, M. Winter and I. Cekic-Laskovic, *Adv. Mater. Interfaces*, 2022, **9**, 2102078.

59 C. Jin, Z. Wu, G. Li, Z. Luo and N.-W. Li, *Acta Phys.-Chim. Sin.*, 2025, 100094.

60 S. G. Stewart, Determination of transport properties and optimization of lithium-ion batteries, PhD thesis, University of California, Berkeley, 2007.

61 C. Chen, Q. Liang, G. Wang, D. Liu and X. Xiong, *Adv. Funct. Mater.*, 2022, **32**, 2107249.